

Bilayer Nanomesh Structures for Transparent Recording and Stimulating Microelectrodes

*Yi Qiang, Kyung Jin Seo, Xuanyi Zhao, Pietro Artoni, Negar H. Golshan, Stanislav Culaclii, Po-Min Wang, Wentai Liu, Katherine S. Ziemer, Michela Fagiolini, and Hui Fang**

Nanomeshed forms of metal have emerged as a promising biocompatible electrode material for future soft bioelectronics. However, metal/electrolyte interfaces are intrinsically capacitive, severely limiting their electrochemical performance, especially for scaled electrodes, which are essential for high-resolution brain mapping. Here, an innovative bilayer nanomesh approach is demonstrated to address this limitation while preserving the nanomesh advantage. Electroplating low-impedance coatings on a gold nanomesh template achieves an impedance < 30 k Ω at 1 kHz and a charge injection limit of 1 mC cm $^{-2}$ for 80 × 80 μm^2 microelectrodes, a 4.3× and 12.8× improvement over uncoated electrodes, respectively, while maintaining a transparency of ≈70% at 550 nm. Systematic characterization of transmittance, impedance, charge injection limits, cyclic charge injection, and light-induced artifacts reveal an encouraging performance of the bilayer nanomesh microelectrodes. The bilayer nanomesh approach presented here is expected to enable next-generation large-scale transparent bioelectronics with broad utility in biology.

electrophysiology to achieve high spatial resolution due to the geometrical inaccessibility of the brain.^[3] Electrophysiology is also “blind” to cell types and to the sophisticated dendrites and axons surrounding neurons.^[4] Novel optical imaging methods, such as epi-fluorescence microscopy and light sheet imaging, can target at single cell and specific cell types, and have generated high-resolution circuitry of the brain.^[5] On the other hand, recently invented optogenetics methods also have excellent spatial resolution with targeted interventions through ion channels and pumps manipulated by light.^[6] Combining optical methods with electrophysiology therefore enables leveraging of the spatial and temporal resolution advantages of both techniques.

By making microelectrodes transparent, light can transmit through the electrode array in both directions to enable simultaneous electrophysiology with optical imaging and optogenetics. In an ideal scenario, transparent microelectrodes should have high transparency, low impedance, high charge injection limit, and low light-induced artifacts at the same time,^[7] ultimately able to distinguish spikes from inhibitory cells or excitatory cells depending on their waveform, or to acquire cortical local field potential (LFP) maps. Among previously developed transparent microelectrodes, indium tin oxide (ITO),^[8] graphene,^[1,4] and metal nanomesh^[9] based microelectrodes demonstrated promising transparency and electrochemical impedances. However, ITO is limited by its brittleness and low conductivity^[10] while the cytotoxicity of graphene remains controversial.^[11] The electrode performance for all three cases are still not sufficient due to their relatively high impedance, especially for scaled microelectrodes. In addition, very limited efforts have been made to make transparent microelectrodes suitable also for electrical stimulation, allowing visualization of underlying neural activities during direct cortical stimulation.^[8c]

In this paper, we present a unique transparent microelectrode material made from a bilayer nanomesh approach via electroplating of low impedance coatings on metal nanomeshes. Such a bilayer nanomesh enables simultaneously low impedance, high charge injection limit, low light-induced artifacts with high transparency, and great mechanical flexibility, which can allow minimally invasive

1. Introduction

Fully decoding the functions of the brain requires simultaneous information on neuronal identity, spatial location, wiring, and firing patterns with great precision.^[1] Electrophysiology has been the gold standard for monitoring brain activity.^[2] While providing high temporal resolution, it has been challenging for

Y. Qiang, K. J. Seo, X. Zhao, Prof. H. Fang
Department of Electrical and Computer Engineering
Northeastern University
Boston, MA 02115, USA
E-mail: h.fang@northeastern.edu

Dr. P. Artoni, Prof. M. Fagiolini
Center for Life Science
Boston Children's Hospital
Boston, MA 02115, USA

N. H. Golshan, Prof. K. S. Ziemer
Department of Chemical Engineering
Northeastern University
Boston, MA 02115, USA

S. Culaclii, P.-M. Wang, Prof. W. Liu
Department of Bioengineering
University of California
Los Angeles, CA 90095, USA

DOI: 10.1002/adfm.201704117

electrical recording/stimulation of the brain concurrent with optical imaging/interventions. Here, we achieved two model low-impedance coatings, namely poly (3,4-ethylene dioxythiophene)-poly (styrene sulfonate) (PEDOT:PSS) and iridium oxide (IrO_x) on pre-formed gold (Au) nanomesh through electroplating. The resulting bilayer nanomeshes allowed drastic improvement of the electrode's impedance and charge injection limit with a minimal decrease in its transparency. As a result, our Au/PEDOT:PSS bilayer nanomesh microelectrodes ($80 \times 80 \mu\text{m}^2$) demonstrated $\approx 10 \text{ k}\Omega$ impedance at 1 kHz and 0.39 mC cm^{-2} charge injection limit, while Au/ IrO_x bilayer nanomesh electrodes ($80 \times 80 \mu\text{m}^2$) achieved around $30 \text{ k}\Omega$ impedance at 1 kHz and 1 mC cm^{-2} charge injection limit, both maintaining over 70% transmittance at 550 nm. Systematic studies on their transmittance, impedance, and charge injection limit revealed that the performance of the bilayer nanomesh microelectrodes can be easily tuned by adjusting the coatings to accommodate requirements for different applications. Detailed cyclic charge-injection tests demonstrated clinically relevant robustness from bilayer nanomesh microelectrodes. Recording with different light intensities also revealed low light-induced artifacts compared to the signal representing neuronal activities for future optical imaging and optogenetics applications. Our results established a promising approach toward next-generation large-scale transparent microelectrodes, with broad utility for applications in neuroscience and therapeutic interventions.

2. Results and Discussion

The synthesis of the bilayer nanomesh starts with fabrication of the Au nanomesh templates, using the procedures described in our previous work.^[9] Briefly, we used a nanosphere lithography method based on self-assembly at the air/water interface for polystyrene spheres (PS) deposition on a given substrate (glass slide or Kapton film). Deposition and lift-off of the Au resulted in the Au nanomesh. Throughout the paper, we used nanomesh templates with a thickness of 15 nm, a width of 70 nm and a pitch of 1 μm unless otherwise noted. A well-established strategy to achieve low impedance and high charge injection limit is to develop low impedance coatings on the electrode surface. Various coating materials have been studied including conducting polymers (CP)^[12] such as PEDOT:PSS,^[13] titanium nitride (TiN),^[14] carbon nanotube (CNT),^[15] and IrO_x .^[16] These materials have either high capacitive or faradaic charge transfer capability, resulting in high charge injection limit as well as low impedance. Here we chose PEDOT:PSS and IrO_x as two model systems, but the same bilayer nanomesh concept can also apply to other coating materials like other conducting polymers and CNT. An electroplating process deposited the PEDOT:PSS and IrO_x coatings on top of Au nanomesh templates. Other ways including spin-coating^[17] and sputtering^[16c,18] can also yield these low impedance coatings. We chose electroplating in this work to achieve the best layer adhesion to Au and compatibility with nanosphere lithography.^[13a,19]

Figure 1a demonstrates the bilayer nanomesh structure, where low impedance coatings are electrodeposited on the Au

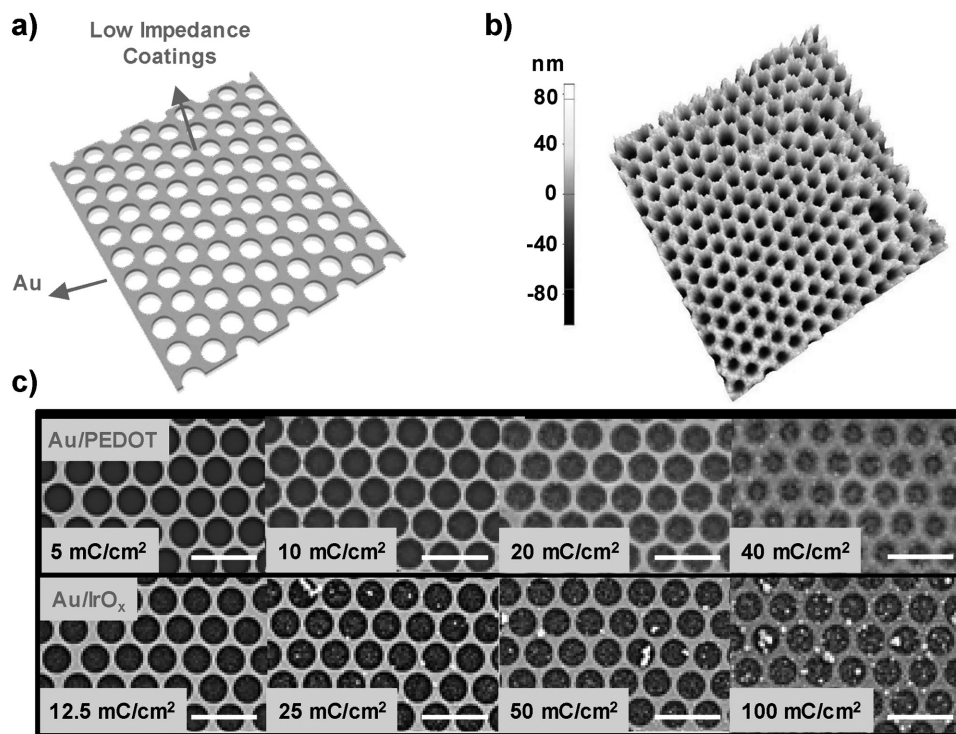


Figure 1. Synthesis and morphology of bilayer nanomeshes (NM) from Au and low-impedance coatings. a) Schematic of a bilayer nanomesh film. b) AFM image of Au/PEDOT:PSS nanomesh. c) Upper row: SEM images of Au/PEDOT:PSS nanomeshes with 5, 10, 20, 40 mC cm^{-2} (left to right) deposition charge density; Lower row: SEM images of Au/ IrO_x nanomeshes with 12.5, 25, 50, 100 mC cm^{-2} (left to right) deposition charge density. Current densities used for electrodeposition are 0.2 mA cm^{-2} for PEDOT:PSS and 0.5 mA cm^{-2} for IrO_x . Scale bar: 2 μm .

nanomesh film. Figure S1 (Supporting Information) illustrates the experimental setup of the electroplating process, which adopted a potentiostat with an Ag/AgCl reference electrode and a Pt counter electrode. For both materials, we adopted galvanostatic deposition for better layer adhesion and uniformity according to previous studies.^[13a,19] For PEDOT:PSS deposition, EDOT monomer was electropolymerized at room temperature by a redox reaction through the current applied to the Au nanomeshes^[20]



While for IrO_x electrodeposition, an Ir complex compound has been proposed to form in the solution at the beginning, which then was anodically oxidized to IrO_2 with slight stoichiometry difference. The process can be described by the following equation^[19]



Current densities for deposition (J_{DEP}) were 0.2 and 0.5 mA cm⁻² for PEDOT:PSS and IrO_x , respectively, while deposition time (t) varied from 0 to 200 s. We observed that high current density was not able to deposit PEDOT:PSS ($J_{\text{DEP}} \geq 0.4 \text{ mA cm}^{-2}$) and IrO_x ($J_{\text{DEP}} \geq 0.8 \text{ mA cm}^{-2}$) nanomesh film with good adhesion, due to high potential (>1 V) on the microelectrodes during electrodeposition. Thus, current density adopted in this work guaranteed good deposition with high efficiency. Details about the electrodeposition process are available in Experimental Section. After the electrodeposition of PEDOT:PSS and IrO_x , we conducted X-ray diffraction (XRD), X-ray photoelectron spectroscopy (XPS), and Raman spectroscopy characterization to determine the formation and crystal composition of the deposited film. The XRD, XPS and Raman results are included in supporting information (Figures S4–S6, Supporting Information). XRD plots revealed a high gold peak at around $2\theta = 38^\circ$. However, the peaks for PEDOT:PSS and IrO_x were small and broad since their crystalline structures are amorphous.^[21,22] XPS survey scan revealed the presence of carbon, oxygen, silicon, and gold in the glass/Au sample represented in the peaks of Figure S5a,b (Supporting Information). In addition, sulfur and Iridium are detectable in PEDOT:PSS and IrO_x resulting coatings, respectively. The surface chemistry of the PEDOT:PSS film shows two types of S 2p bonding on the sample (Figure S5c, Supporting Information). The higher binding energy peak around 168 eV was contributed by the sulfur atoms in PSS, whereas the peak at lower binding energy (164 eV) was likely the sulfur atom in PEDOT. Furthermore, the Ir 4f peak on the IrO_x film on gold shown in Figure S5d (Supporting Information), shows the Ir 4f_{7/2} and Ir 4f_{5/2} peak energies of 62 and 65 eV, respectively, very close to the value expected for IrO_2 (62.35 and 65.35 eV). Figure S6a,b (Supporting Information) show Raman spectra of Au/PEDOT:PSS and Au/ IrO_x , respectively. For Au/PEDOT:PSS, dominant peaks were observed at 1366, 1438, 1496, and 1569 cm⁻¹ along with smaller peaks at 435, 529, and 985 cm⁻¹, which agree well with other literature.^[21] The Raman on electroplated Au/ IrO_x shows a small broad peak (E_g) at around 576 cm⁻¹, which shows similar measurements with other literature.^[22]

To shed light on electroplated coating process on the nanomesh templates, we examined the microstructures of the bilayer nanomesh samples using atomic force microscopy (AFM) and scanning electron microscope (SEM). Figure 1c displays the SEM images of samples with different electroplating charge densities (σ_{DEP} , that is, deposition time t times J_{DEP}). Intriguingly, we found that the entire coating process roughly separated into two stages as increasing deposition charge density, namely templated electroplating, followed by full film electroplating when a continuous coating inside holes were formed. As shown in the SEM, the morphology of Au/PEDOT:PSS nanomeshes appeared almost the same as the uncoated one, suggesting nearly templated electroplating after up to 10 mC cm⁻² deposition, which yielded bilayer nanomeshes with the same top and bottom layers' widths. As charge density increased, small particles started to emerge from the metal edges and occupy more in the nonmetal area (i.e., the substrate). At $\sigma_{\text{DEP}} = 30 \text{ mC cm}^{-2}$, they eventually yielded a continuous film of PEDOT:PSS inside the holes. The trend was similar for IrO_x with particles appearing around the metal lines. At $\sigma_{\text{DEP}} = 75 \text{ mC cm}^{-2}$, the IrO_x formed a thin film inside the holes. SEM images of Au/PEDOT:PSS and Au/ IrO_x nanomeshes with higher resolution are available in Figure S2 (Supporting Information), showing detailed morphologies of the bilayer nanomeshes. PEDOT:PSS tends to have a better templated deposition than IrO_x does. The AFM images are in good agreement with the SEM results. Figure 1b shows AFM image of bilayer structure of Au/PEDOT:PSS. Templated electroplating was successful as PEDOT:PSS layer after 0.2 mA cm⁻², 50s deposition. And it has been observed PEDOT:PSS nanomesh has a rough surface. However, as shown in Figure S3 (Supporting Information), IrO_x particles grow on the nonmetal area after 0.5 mA cm⁻², 75s deposition. AFM image of Au nanomesh film is also shown in Figure S3 (Supporting Information) as a control. Growth rates of PEDOT:PSS and IrO_x layers were also determined by thickness profiles derived from AFM from samples with an effective coating area of 1–2 cm². As a result, the deposition rate of PEDOT:PSS on 15 nm thick gold is 1.7 nm s⁻¹ and that of IrO_x is 1.3 nm s⁻¹. We attribute the formation of thin layer in the nonmetal holes to the lateral growth of materials from the side area of Au nanomesh. Changes in solution pH, temperature, agitation and sonication appeared to have negligible effects on the lateral growth of IrO_x . Ongoing studies are investigating how to minimize the lateral growth to elongate the templated electroplating stage.

Optical transmittance of the bilayer nanomeshes matches with their microstructures. Figure 2a,b illustrates transmittance spectrum in the wavelength range from 400 to 1100 nm for Au/PEDOT:PSS and Au/ IrO_x nanomeshes, respectively. The deposition charge densities was 0, 10, 20 and 40 mC cm⁻² for PEDOT:PSS ($J_{\text{DEP}} = 0.2 \text{ mA cm}^{-2}$) and 0, 25, 50 and 100 mC cm⁻² for IrO_x ($J_{\text{DEP}} = 0.5 \text{ mA cm}^{-2}$). As expected, the transmittance decreases as deposition charge density since more materials are coated. Figure 2c,d plots transmittance at 550 nm as a function of deposition charge density for the two bilayers. Notably, for both bilayers, their transmittance dropped nonlinearly as charge density with the first region being slow decrease (less than 1% of transmittance decrease per 2 mC cm⁻² of PEDOT:PSS deposition or

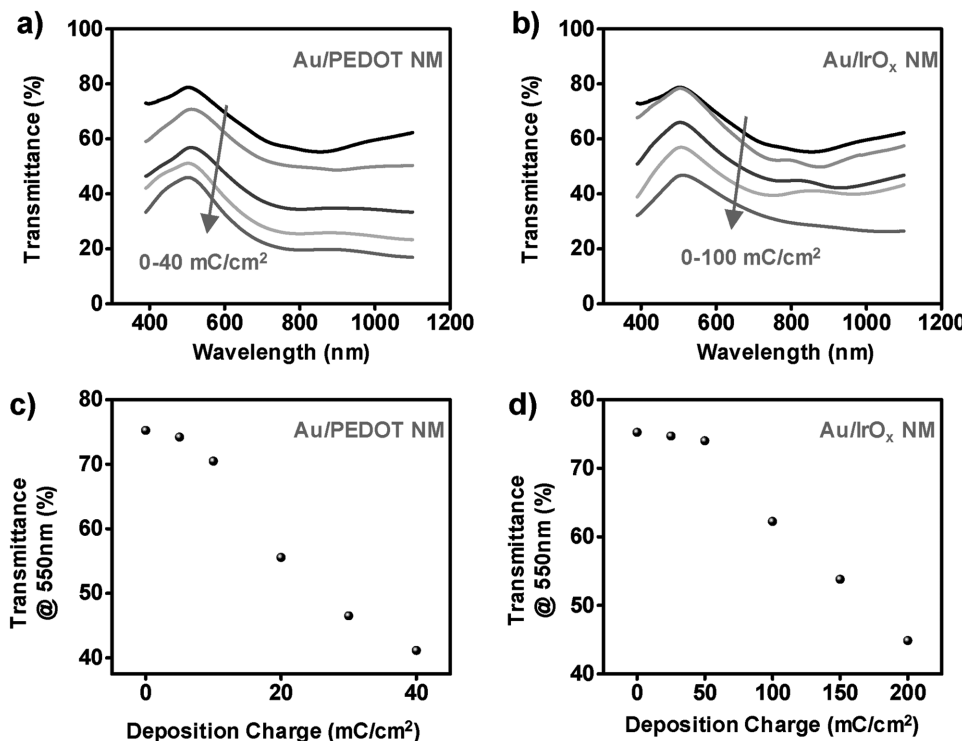


Figure 2. Optical transmittance of bilayer nanomeshes. a) Transmittance spectrum of Au/PEDOT:PSS nanomeshes with different deposition charge densities. b) Transmittance spectrum of Au/IrO_x nanomeshes with different deposition charge densities. c) Transmittance of Au/PEDOT:PSS nanomeshes at 550 nm versus deposition charge densities. d) Transmittance of Au/IrO_x nanomeshes at 550 nm versus deposition charge densities.

per 5 mC cm^{-2} of IrO_x deposition), and the second one fast dropping ($\approx 2\%$ of transmittance decrease per 2 mC cm^{-2} of PEDOT:PSS deposition or per 5 mC cm^{-2} of IrO_x deposition). This phenomenon coincided well with the two-stage coating process we observed from SEM, with the turning points in deposition charge density also match each other. Overall, Au/IrO_x nanomeshes showed higher transmittance than Au/PEDOT:PSS even with larger deposition charge density. It was shown that the bilayer nanomeshes maintained over 70% transmittance at 550 nm with PEDOT:PSS from up to 10 mC cm^{-2} , and with IrO_x from up to 37.5 mC cm^{-2} electroplating.

As expected, the electroplating of PEDOT:PSS and IrO_x significantly improves the electrochemical performance of the microelectrode. Figure 3 shows the detailed electrochemical impedance (EIS) and charge storage capacity (CSC) characterization of the bilayer nanomesh microelectrodes. For all electrochemical characterization, we used electrodes with $80 \times 80 \mu\text{m}^2$ windows if not specifically mentioned. Figure 3a illustrates a schematic of the device with a bilayer nanomesh microelectrode interconnected with a Au nanomesh (thickness, 15 nm), with SU-8 as an encapsulation layer (thickness, 4 μm) and Kapton film (thickness, 25 μm) as a substrate. Same fabrication process yielded microelectrodes on a variety of substrates, including glass, Kapton, and parylene. As shown in Figure 3b,c, the impedances of both Au/PEDOT:PSS and Au/IrO_x nanomesh microelectrodes decreased as the deposition charge density in the entire measurement frequency range from 100 Hz to 100 kHz. The impedance at 1 kHz is a common metric for assessing the electrochemical performance of microelectrodes.

If we target for 70% transmittance at 550 nm, the impedance of Au/PEDOT:PSS nanomesh electrodes at 1 kHz achieved $\approx 10 \text{ k}\Omega$, while that of Au/IrO_x nanomesh electrodes reached $\approx 30 \text{ k}\Omega$. With similar transmittance, the impedance of Au/PEDOT:PSS microelectrodes is smaller than that of Au/IrO_x microelectrodes, which could arise from the electrochemical properties, thickness, and surface roughness differences of these two coatings. Compared to the $180 \text{ k}\Omega$ electrode impedance before coating, the significant decrease of impedance is resulted from the larger effective surface area (ESA) and lower faradaic charge transfer resistance after coating. Thicker coating has a larger ESA due to larger surface roughness and extended surface area, causing a further decrease in the impedance.

Impedance at 1 kHz as a function of deposition charge density for both bilayer nanomesh electrodes is shown in Figure S9c, d (Supporting Information). Even from the templated electroplating stage the coatings already showed drastic improvement on electrode impedance, while the boundaries between the two stages were not obvious from the impedance trends. Impedance phase spectra of both bilayer nanomesh electrodes confirmed the faradaic nature of the electrode/electrolyte interface (Figure S9a,b, Supporting Information). In previous work, we observed that bare Au nanomesh electrode had a highly capacitive surface with a phase angle of -80° .^[9] However, phase angle gradually increased to -20° after coating, indicating a more faradaic electrode–electrolyte interface. This improved interface and impedance significantly enhanced signal recording. White noise (thermal noise), a nonnegligible source of interference during neural signal

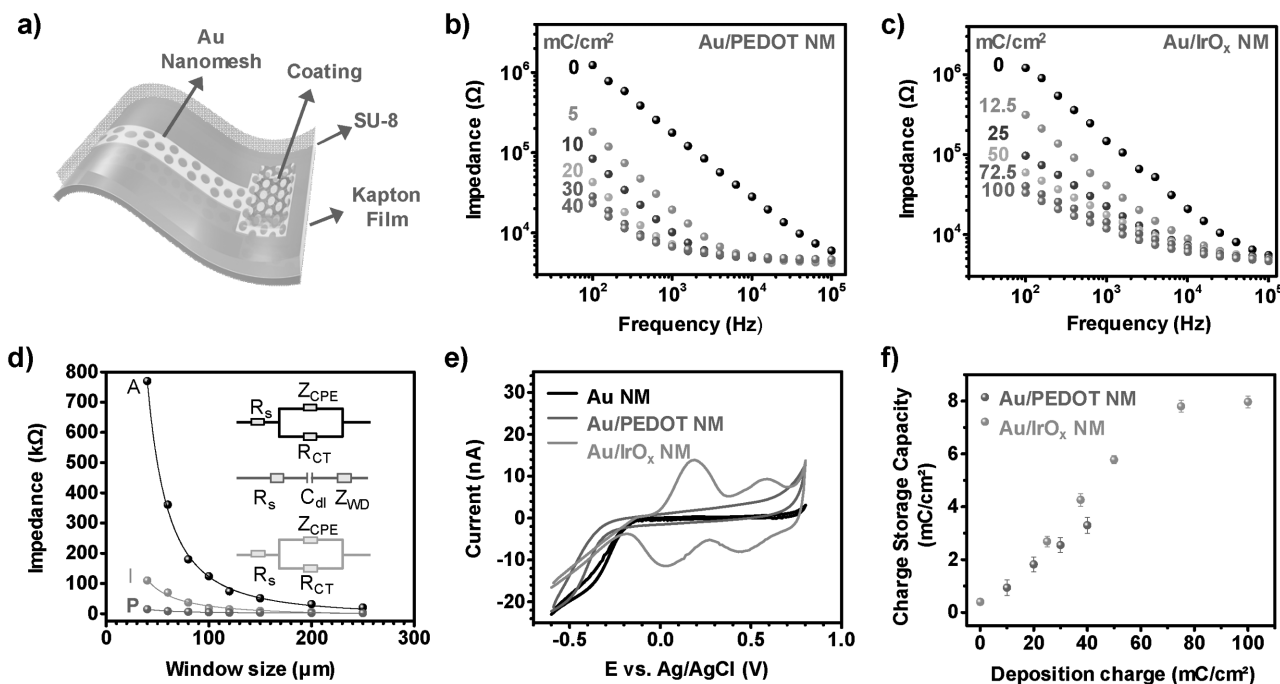


Figure 3. Electrochemical characterization of bilayer nanomesh microelectrodes. a) Schematic diagram of bilayer nanomesh microelectrode ($80 \times 80 \mu\text{m}^2$) with Kapton (thickness, 25 μm), Au (thickness, 15 nm), and SU-8 (thickness, 4 μm). b) Impedance spectra of Au/PEDOT:PSS nanomesh microelectrodes with different deposition charge densities. c) Impedance spectra of Au/IrO_x nanomesh microelectrodes with different deposition charge densities. d) Impedance at 1 kHz versus electrode sizes for Au, Au/PEDOT:PSS ($\sigma_{\text{DEP}} = 30 \text{ mC cm}^{-2}$), Au/IrO_x ($\sigma_{\text{DEP}} = 37.5 \text{ mC cm}^{-2}$) nanomesh microelectrodes. Inset shows specific equivalent circuit models used for electrode–electrolyte interface of each microelectrode. Here A,I,P represent Au, Au/IrO_x, Au/PEDOT:PSS nanomesh, respectively. e) Cyclic voltammetry results of Au, Au/PEDOT:PSS ($\sigma_{\text{DEP}} = 30 \text{ mC cm}^{-2}$), Au/IrO_x ($\sigma_{\text{DEP}} = 37.5 \text{ mC cm}^{-2}$) nanomesh microelectrodes. f) Charge storage capacity of Au/PEDOT:PSS, Au/IrO_x nanomesh microelectrodes versus deposition charge density.

recording, decreased drastically with lower electrode impedance (Figure S10a, Supporting Information). The coated electrodes showed clearly smaller peak-to-peak noise amplitude than bare Au nanomesh microelectrodes. Root-mean-square (rms) noise calculated from bare Au, Au/PEDOT:PSS ($\sigma_{\text{DEP}} = 10 \text{ mC cm}^{-2}$) and Au/IrO_x ($\sigma_{\text{DEP}} = 37.5 \text{ mC cm}^{-2}$) nanomesh microelectrodes was 8.2, 3.8, and 4.7 μV , respectively. Both bilayer nanomesh electrodes chosen here have over 70% transmittance. Power spectra density (PSD) of noise recording were also available in the supporting information (Figure S10b, Supporting Information), showing the same trend as the time domain data.

Figure 3d shows the 1 kHz impedance of Au, Au/PEDOT:PSS, and Au/IrO_x nanomesh microelectrodes as a function of electrode sizes. The deposition charge density used was 30 mC cm⁻² for PEDOT:PSS and 37.5 mC cm⁻² for IrO_x, which were chosen for both bilayer nanomesh microelectrodes to have same charge injection limit of 1 mC cm⁻². We also fitted the data with an equation model: $Z = a + bA^{-c}$. Here variable Z is the impedance, A is the electrode window area (L^2 , where L is the size of the electrode), and a, b, and c are fitting parameters. The power factor c indicates how the impedance changed with different electrode sizes. While the impedance of Au nanomesh microelectrodes had a near-precise 1/A trend, which we have explained previously due to capacitive interface,^[9] the relationship for both PEDOT:PSS and IrO_x coated microelectrodes showed $\approx 1/A^{0.74}$, $1/A^{0.69}$ respectively, very different from the Au case. To elucidate the interfacial properties at the electrode–electrolyte interfaces, we performed

circuit modeling to fit the impedance spectrum. The inset of Figure 3d shows specific equivalent circuit models used for the electrode–electrolyte interface of Au, Au/PEDOT:PSS, and Au/IrO_x nanomesh microelectrodes (from up to down). To find the most appropriate model for each interface, we fitted the electrochemical impedance data with several existing resistance-capacitance (R-C) models for the electrode–electrolyte interface in literature.^[1,13b,20,23] We adopted circuit models with the best goodness of fitting. Elements used in circuit models included series resistance (R_s), double-layer capacitance (C_{dl}), charge-transfer resistance (R_{CT}), and Warburg element for diffusion (W_D). For Au/PEDOT:PSS, we used the model where W_D and double-layer capacitance (C_{dl}) are in series,^[20] while for uncoated Au and Au/IrO_x nanomesh electrodes, we used models with parallel R_{CT} and C_{PE} . R_s resulted from the solution resistance, which was always in series with other elements. Details of fitting parameters for different nanomesh microelectrodes appear in the supporting information (Figures S12–S14, Supporting Information). For Au nanomesh microelectrodes, as shown in Figure S12 (Supporting Information), we calculated the contribution of impedance from different circuit elements. With the large R_{CT} ($\approx M\Omega$) and small impedance from C_{PE} ($\approx k\Omega$) in parallel, the overall impedance should be dominated by C_{PE} , showing an 1/A dependence. Also, as we know, the impedance of C_{PE} equals $\frac{1}{Y_0(j\omega)^n}$, where Y_0 has the numerical value of the admittance ($1/|Z|$) at $\omega = 1 \text{ rad s}^{-1}$, and the unit of Y_0 is $S \times s^n$.

The phase angle of C_{PE} has a value of $-(90 \times n)$ degrees, with n usually ranging from 0 to 1. With $n = 0$, it describes a pure resistor while with $n = 1$, it represents an ideal capacitor. With n close to 1 (≈ 0.92), C_{PE} represented a pure capacitor in this case, indicating a nearly ideal double-layer capacitive interface of Au nanomesh microelectrodes. For Au/PEDOT:PSS nanomesh microelectrodes, we used another model as we mentioned, where R_S , C_{dl} , and W_D are in series. From the impedance of different elements we calculated in Figure S13 (Supporting Information), it is clear that the overall impedance was not dominated by C_{dl} anymore. The contribution from W_D must be accounted for to the calculation of impedance. When electrodes size became large enough, even R_S took an important role in the overall impedance. With the combination of R_S , C_{dl} , and W_D , the power factor c equals 0.74 in this case. For Au/IrO_x nanomesh microelectrodes, same circuit model as Au nanomesh microelectrodes fit the data the best. It is clearly seen that R_{CT} significantly decreased after deposition. However, from the table in Figure S14 (Supporting Information), one can see R_{CT} is still over 10 times larger than the impedance calculated from C_{PE} , suggesting that C_{PE} is still dominating the overall impedance as they are in parallel. But with n decreasing from 0.92 to 0.68 after deposition, C_{PE} no longer represented a pure capacitor. The fitted power factor c became 0.69, showing a more faradaic interface here.

To reveal further details about the faradaic interfaces of the bilayer nanomesh, we studied the nanomesh microelectrodes through cyclic voltammetry (CV) measurements. CV measurements of Au, Au/PEDOT:PSS and Au/IrO_x nanomesh microelectrodes all adopted 50 mV s⁻¹ scan rate and cyclic voltage range from -0.6 to 0.8 V, which is the well-established voltage window to prevent water electrolysis (water window). CV results of uncoated Au, Au/PEDOT:PSS ($\sigma_{DEP} = 30 \text{ mC cm}^{-2}$) and Au/IrO_x ($\sigma_{DEP} = 37.5 \text{ mC cm}^{-2}$) nanomesh microelectrodes appear in Figure 3e. The enclosed area of each CV curve defines the charge storage capacity (CSC) of the microelectrodes. From Figure 3e, it is clear that the CSC value increases significantly after both PEDOT:PSS and IrO_x coatings. The CSC derived from curves in Figure 3e is 0.4 mC cm⁻² for Au nanomesh microelectrodes, 2.55 mC cm⁻² for Au/PEDOT:PSS nanomesh microelectrodes ($\sigma_{DEP} = 30 \text{ mC cm}^{-2}$) and 4.3 mC cm⁻² for Au/IrO_x nanomesh microelectrodes ($\sigma_{DEP} = 37.5 \text{ mC cm}^{-2}$), respectively. Figure 3f plots the CSC of Au/PEDOT:PSS and Au/IrO_x nanomesh microelectrodes as a function of different deposition charge density. The CSC of both bilayer nanomesh microelectrodes increased with more deposition, which resulted from larger ESA after coating. Similar to the impedance trends, the CSC plots did not show obvious stage boundaries.

Next, we evaluated the electrical stimulation capability of the bilayer nanomesh microelectrodes. In electrical stimulation using microelectrodes, electrodes will be polarized in the electrode-electrolyte system when current pulses are applied. Once the electrode/electrolyte interface reaches certain voltage values, irreversible faradaic reaction will happen, causing damage to electrodes and surrounding tissues, along with pH changes and unwanted chemical products.^[12] Most common irreversible faradaic reaction is the oxidation and reduction of water. Thus, the definition of charge injection limit (CIL) is the amount of charge needed to polarize electrode to the boundaries of water

hydrolysis window. Both CSC and CIL indicate the charge transfer capability of electrodes, while CIL is a more practical metric for electrical stimulation since real stimulation applications require sub-millisecond pulse duration, which equals over 100 000 mV s⁻¹ charge transfer rate, much faster compared to the value (50 mV s⁻¹) used for CV measurements. But the increase in CSC will normally improve the CIL as well, and these two parameters are related by a stimulus efficiency.

We indeed observed great improvements in the CIL from both bilayer nanomesh microelectrodes. We performed voltage transient measurement to derive the CIL of Au/PEDOT:PSS and Au/IrO_x nanomesh microelectrodes. Figure 4a displays voltage transients of Au, Au/PEDOT:PSS ($\sigma_{DEP} = 30 \text{ mC cm}^{-2}$) and Au/IrO_x ($\sigma_{DEP} = 37.5 \text{ mC cm}^{-2}$) nanomesh microelectrodes under a cathodic first, charge balanced, symmetric biphasic current pulse of 500 μs , 128 μA (1 mC cm⁻²) with 0.6 V positive bias. The bilayer nanomesh microelectrodes both demonstrated much smaller polarization than bare Au nanomesh microelectrodes when applying the same amount of charge to them, showing much higher charge injection capability. To extract the CIL from the voltage transient curve, we compared the most negative voltage (E_{mc}) and most positive voltage (E_{ma}) of the microelectrode with the water hydrolysis window (0.6 V, -0.8 V).^[7a] Either E_{mc} below -0.6 V or E_{ma} above 0.8 V will be considered unsafe in neural stimulation. Using protocols mentioned in the Experimental Section, we extracted the CIL of bilayer nanomesh microelectrodes as a function of different deposition charge densities (Figure 4b). The CIL of both bilayer nanomesh microelectrodes increased with more deposition in a trend similar to CSC and eventually saturated. Overall, the CIL reached 0.39 mC cm⁻² for Au/PEDOT:PSS nanomesh microelectrodes and 1 mC cm⁻² for Au/IrO_x ones, while still preserving over 70% transmittance at 550 nm. Although the requirement of charge injection limit depends on applications, it has been suggested that microelectrodes with 1 mC cm⁻² will be enough for high-density microstimulation with good spatial resolution and site specificities.^[24] In this case, Au/PEDOT:PSS nanomesh microelectrodes will have some limitations in high-density stimulation, but still has a better performance than conventional metallic multielectrode arrays (MEAs) used for neural stimulation (usually 0.05–0.3 mC cm⁻²),^[13b] while Au/IrO_x nanomesh microelectrodes demonstrated both high charge injection limit and transparency. Also, more deposition can always enhance the performance, if less transparency is tolerable. In Table 1, we summarized the transmittance, impedance, and charge injection limit of Au/PEDOT:PSS and Au/IrO_x nanomesh microelectrodes under several different deposition conditions to illustrate the trade-off between those three key performances. We also benchmarked the performance of our bilayer nanomesh microelectrode against previous transparent microelectrodes, detailed in Table 1. The bilayer nanomesh microelectrodes demonstrated comparable transmittance, with orders of magnitude improvements in the impedance and charge injection limits. The Au nanomesh also showed much lower sheet resistance compared to graphene or ITO according to our previous work.^[9] The CIL reached 1 mC cm⁻² for bilayer nanomesh microelectrodes with 0.2 mA cm⁻², 150 s PEDOT:PSS or 0.5 mA cm⁻²–75 s IrO_x coating. As is evident from the high-resolution SEM and AFM images, the

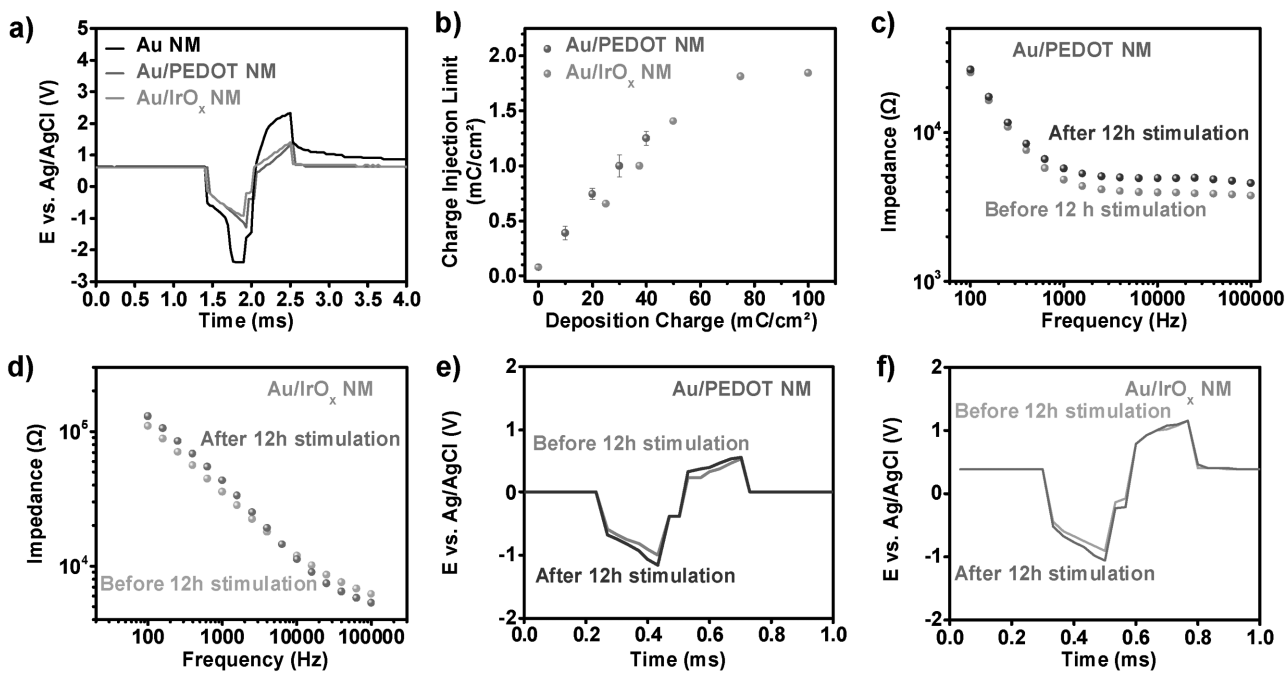


Figure 4. Charge injection characterization and reliability of bilayer nanomesh microelectrodes. a) Voltage transients of Au, Au/PEDOT:PSS ($\sigma_{DEP} = 30 \text{ mC cm}^{-2}$), Au/IrO_x ($\sigma_{DEP} = 37.5 \text{ mC cm}^{-2}$) nanomesh microelectrodes ($80 \times 80 \mu\text{m}^2$) under $500 \mu\text{s}$, $128 \mu\text{A}$ (1 mC cm^{-2}) cathodic first, biphasic current pulse. b) Charge injection limit of Au/PEDOT:PSS, Au/IrO_x nanomesh microelectrodes versus deposition charge density. c) Impedance spectra of Au/PEDOT:PSS ($\sigma_{DEP} = 30 \text{ mC cm}^{-2}$) nanomesh microelectrodes under $200 \mu\text{s}$, $120 \mu\text{A}$ (0.375 mC cm^{-2}) cathodic first, biphasic current pulse before/after 12 h stimulation. d) Impedance spectra of Au/IrO_x ($\sigma_{DEP} = 37.5 \text{ mC cm}^{-2}$) nanomesh microelectrodes under $200 \mu\text{s}$, $120 \mu\text{A}$ (0.375 mC cm^{-2}) cathodic first, biphasic current pulse before/after 12 h stimulation. e) Voltage transient of Au/PEDOT:PSS ($\sigma_{DEP} = 30 \text{ mC cm}^{-2}$) nanomesh microelectrodes under $200 \mu\text{s}$, $120 \mu\text{A}$ (0.375 mC cm^{-2}) cathodic first, biphasic current pulse before/after 12 h stimulation. f) Voltage transient of Au/IrO_x ($\sigma_{DEP} = 37.5 \text{ mC cm}^{-2}$) nanomesh microelectrodes under $200 \mu\text{s}$, $120 \mu\text{A}$ (0.375 mC cm^{-2}) cathodic first, biphasic current pulse before/after 12 h stimulation.

PEDOT:PSS and IrO_x layers are composed of nanoparticles with sizes ranging from 20 to 30 nm. We expect these nanoparticles to increase the effective surface area of the microelectrode, to therefore decrease its impedance and increase its charge injection limit. In addition, we have derived a large-signal bioimpedance equivalent-circuit model of the electrode to describe the

electrode potential response to a current stimulation in time domain. The model is calculated from stimulation waveforms in Figure 4a, based on the methodology presented previously.^[25] It is based on electrode response to stimulation current during reversible charge transfer at the electrode interface, where the potential does not exceed the water window. Traces for PEDOT and IrO_x coated electrodes in Figure 4a were used for our derivation, while uncoated Au electrode showed overstimulation behavior and was thus not used for calculations. Importantly, the resulting large-signal models for PEDOT and IrO_x can be used to predict the electrode potential waveform to an injected stimulation pulse with arbitrary amplitude and time duration parameters, and indicate whether it will exceed the water window. The derived model parameters are recorded in Figure S15 (Supporting Information). These parameters show a good match to EIS-based model. But unlike the small-signal EIS model, the circuit topology of this model is better suited to describe the large-signal stimulation waveforms in time domain.

On the other hand, it is essential to have long-term stability of the electrodes during continuous stimulation without significant delamination of materials. In this work, both Au/PEDOT:PSS ($\sigma_{DEP} = 30 \text{ mC cm}^{-2}$) and Au/IrO_x ($\sigma_{DEP} = 37.5 \text{ mC cm}^{-2}$) nanomesh microelectrodes were continuously stimulated using clinically relevant current pulse train of $200 \mu\text{s}$, $120 \mu\text{A}$ (0.375 mC cm^{-2}) at 50 Hz for 12 h , corresponding to over 2.1 million pulses. Impedance magnitude

Table 1. Current transparent microelectrodes with different specifications on transmittance (T), impedance (Z) and charge injection limit (Q_{inj}).

Microelectrode material	T [%]	Z [$k\Omega$]	Microelectrode size [μm^2]	Q_{inj} [mC cm^{-2}]
Graphene ^[1]	95	243.5 ± 5.9	31400	–
Doped graphene ^[4]	95	541	2500	–
ITO-PET ^[8c]	80	10–50	49062.5	–
Au nanomesh ^[9]	74	127.19	6400	–
Au/PEDOT:PSS nanomesh	70.48	10.55 ± 1.56	6400	0.39 ± 0.06
	55.54	8.13 ± 1.85	6400	0.75 ± 0.05
	46.50	6.71 ± 1.02	6400	1.00 ± 0.10
Au/IrO _x nanomesh	74.02	35.55 ± 12.7	6400	0.66 ± 0.06
	70.21	30.01 ± 10.30	6400	1.00 ± 0.07
	62.24	24.74 ± 7.50	6400	1.41 ± 0.08

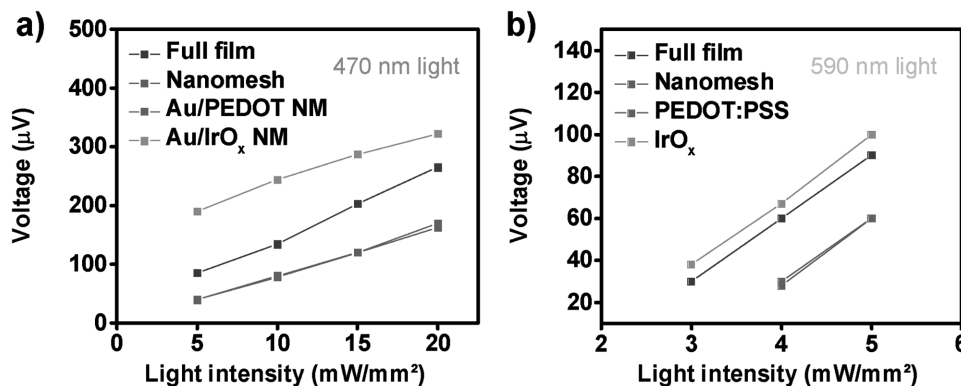


Figure 5. Light-induced artifacts characterization. Light-induced artifacts of Au full film, Au nanomesh, Au/PEDOT:PSS nanomesh ($\sigma_{DEP} = 10 \text{ mC cm}^{-2}$), Au/IrO_x nanomesh ($\sigma_{DEP} = 37.5 \text{ mC cm}^{-2}$) microelectrodes versus light intensity using a) 470 nm blue light and b) 590 nm amber light.

spectrum of bilayer nanomesh microelectrodes before and after 12 h stimulation is shown in Figure 4c,d. After 12 h stimulation, the impedance at 1 kHz only increased by 1 and 8 kΩ for Au/PEDOT:PSS and Au/IrO_x nanomesh microelectrodes, respectively. Figure 4e,f illustrate voltage transients before and after the 12 h stimulation. There were minimal changes in E_{mc} and E_{ma} for both bilayer microelectrodes, highlighting clinically relevant robustness. Besides the electrochemical stability, mechanical flexibility of a transparent microelectrode is also of great importance. In this work, we performed bending tests with both Au/PEDOT:PSS and Au/IrO_x nanomesh microelectrodes. Figure S8 (Supporting Information) demonstrates the impedance change after up to 500 bending cycles with a bending radius of 4 mm. There was only slight change of impedance after 500 cycles bending, indicating the excellent flexibility of our devices.

Light-induced artifacts present certain challenges when using transparent microelectrodes for optogenetic applications.^[7b,26] When the light with energy higher than the work function of a metal shines on it, electrons will emit causing photoelectric effects. In electrode and electrolyte system, the effective work function of metal will decrease, which makes it easier to have artifacts with even longer wavelength light. The resulted artifacts can interfere with local field potentials (LFP), posing difficulty to distinguish artifacts from neural signals.^[26] We measured the light-induced artifacts by immersing electrodes into PBS solution while using a platinum (Pt) wire as a reference electrode. We also used a grounded Faraday cage to suppress environmental noises for a better recording. We then used a fiber-coupled LED to deliver light of two different wavelengths, 470 nm (blue) and 590 nm (amber). By attaching the fiber tip on the microelectrode surface, artifacts were quantified from noise recording in the form of potential peaks. We studied the dependence of the amplitude of artifacts on different light intensity using a 5 ms pulse duration. A power meter measured the light intensity used here, which ranged from 5 to 20 mW mm⁻² for blue light and 1 to 5 mW mm⁻² for amber light with same driving current. Relevant results are shown in Figure 5a,b, including artifacts measured from Au full film, Au nanomesh, Au/PEDOT:PSS nanomesh ($\sigma_{DEP} = 10 \text{ mC cm}^{-2}$) and Au/IrO_x nanomesh ($\sigma_{DEP} = 37.5 \text{ mC cm}^{-2}$) microelectrodes (200 × 200 μm²). Only artifact values greater than the noise

floor (~20 μV peak-to-peak) were presented. As expected, the artifacts increased with higher light intensity due to stronger photoelectric effects.

We observed that Au nanomesh microelectrodes have much less artifacts than Au full-film microelectrodes, largely due to less metal inside the same electrode window. For example, using 5 mW mm⁻² blue light, artifacts measured from Au full-film microelectrodes were ~100 μV while those from Au nanomesh microelectrodes were only about 40 μV, highlighting the nanomesh advantage. Au/PEDOT:PSS nanomesh microelectrode had similar artifacts with Au nanomesh microelectrodes, suggesting that coating PEDOT:PSS did not add more artifacts. The artifacts of Au/PEDOT:PSS nanomesh microelectrodes also did not change with more deposition of PEDOT:PSS (Figure S16a, Supporting Information). On the other hand, Au/IrO_x nanomesh microelectrodes had larger artifacts than other microelectrodes, possibly due to the light absorption in defects in IrO_x, which lead to photocarrier generation. This phenomenon was also consistent with the fact that Au/IrO_x nanomesh microelectrodes had relatively linear increase of artifacts with more deposition (from Figure S16b, Supporting Information). These trends were in agreement with previous reports that PEDOT:PSS was artifact-free at least at these wavelengths,^[7b] and our interpretation that IrO_x itself was light absorbing and generated artifacts. Further studies can explore optimization of the electronic structure of IrO_x to minimize this artifact. We note that these artifacts only emerge at large illumination intensity (above 1 mW mm⁻²), while it is not an issue for regular optical imaging, such as diffuse optical tomography (DOT), which requires only an average of 0.128 mW mm⁻² light intensity at each wavelength.^[27] For applications with strong illumination, the Au/PEDOT:PSS nanomesh microelectrode is a promising choice for its reduced artifacts.

3. Conclusion

In this paper, we coined and successfully demonstrated a bilayer nanomesh approach via Au/PEDOT:PSS and Au/IrO_x nanomeshes from electroplating of PEDOT:PSS and IrO_x coatings on preformed Au nanomesh templates. The coating process was found to follow first a templated electroplating stage

then a full film electroplating stage. Microelectrode from the bilayer nanomeshes demonstrated promising performance in transmittance, impedance and charge injection limit, even with coatings from the initial templated electroplating stage. These performances were also easily adjustable by tweaking the thickness of these electroplated materials. Ongoing efforts are investigating the tuning of deposition process to suppress the lateral growth to further increase the performance limit from the bilayer nanomesh microelectrodes. Further studies will also develop large-scale microelectrode arrays from these bilayer nanomesh materials for *in vivo* brain-mapping with concurrent optical imaging and optogenetic interventions. We also envision that with proper mesh design, such a bilayer nanomesh system will be suitable for high performance, stretchable neuroelectrodes, enabling large scale, chronically implantable neural interfaces.

4. Experimental Section

Materials and Tools: Polystyrene spheres (carboxyl latex bead, 4% w/v, 1.0 μm in diameter) were from Thermo Fisher Scientific. Ethylene dioxythiophene (EDOT) monomer and poly(styrene sulfonate) sodium salt (NaPSS) powder were from Sigma-Aldrich. Iridium chloride (IrCl_4) was from Alfa Aesar. Hydrogen peroxide (H_2O_2), oxalic acid dihydrate, and anhydrous potassium carbonate (CK_2O_3) were from Fisher Scientific. All materials were used as received. Scanning electron microscope (Supra 25 SEM) was used to characterize the structure of uncoated and coated bilayer nanomesh. Atomic force microscopy (Parks Scientific XE7 AFM) and X-ray diffraction (PANalytical/Philips X'Pert Pro) were used for surface morphology and molecular structure of crystal characterization, respectively. X-ray photoelectron spectroscopy (XPS) consisted of a Mg/Al dual-anode nonmonochromated X-ray source (Phi model 04-548) and a hemispherical analyzer (Phi model 10-360). The two X-ray options were Mg $\text{K}\alpha$ (1253.6 eV) and Al $\text{K}\alpha$ (1486.6 eV) operated at 300 W. The system was calibrated using Au 4f and Cu 2p, and had a minimum full width half maximum (FWHM) of 1.5 eV with an 80% Gaussian/Lorentzian distribution at a pass energy of 35.75 eV. XPS analysis revealed the chemical composition of a 1 mm circle of the surface to a depth of ≈ 10 nm at a 90° take-off angle.vcx.

Fabrication of Gold Nanomesh: To deposit PS nanospheres on a substrate, an air/water interface with self-assembly method was used as previously described.^[9] After achieving the PS self-assembled monolayer, inductively coupled plasma-reactive ion etching (ICP-RIE) with O_2 and CHF_3 gases trimmed the spheres smaller. The etching time was 40 s with 40 sccm of O_2 , 2 sccm of CHF_3 , pressure of 25 mT, 100 W for radio frequency power 1 (RF₁) and 150 W for RF₂. For metal deposition, 1 nm of Cr and 15 nm of Au were deposited at the rate of 0.5 and 1 A s⁻¹, respectively, using e-beam evaporation for easier lift-off. Sonication of the samples in chloroform for 2 min produced gold nanomeshes on a substrate.

Fabrication of Gold Nanomesh Microelectrodes: Using the fabricated nanomesh samples above, a positive photoresist (S1818, Shipley) spin-coated the nanomesh using 4000 rpm for 45 s. Then, using photolithography technique, we defined microelectrode and interconnect patterns with UV exposure and development, followed by wet etching of Au and Cr, using Au etchant and Cr etchant, respectively. Sonication of the samples in acetone completely removed the remaining photoresist. As an insulation layer, SU-8 2005 (Microchem) spin-coated the patterned sample using 4000 rpm for 30 s for contact area isolation, resulting 4 μm in thickness. After soft baking at 95 °C for 2 min, the sample went through UV exposure of 6 s, followed by a post exposure bake of 3 min

at 95 °C. For development, sonication in SU-8 developer for 20 s and rinsing with fresh SU-8 developer and the IPA produced clear isolation patterns. Hard baking at 200 °C for 20 min completed the process. The fabricated microelectrode had a 10 mm length, a 300 μm width, and a 2 \times 3 mm² contact pad size.

Electrodeposition of IrO_x and PEDOT:PSS: Poly(3,4-ethylene dioxythiophene)-poly (styrene sulfonate) (PEDOT:PSS) solution was prepared by mixing ethylene dioxythiophene (EDOT) monomer (0.01 M) and poly(styrene sulfonate) sodium salt (NaPSS) powder (0.1 M) in deionized water (150 mL) and stirring for 30 min.^[13a] 0.2 mA cm⁻² constant current was applied using galvanostatic mode. Different deposition charge from 25 to 200 s was applied in order to study the transmittance and electrical performance of PEDOT:PSS-coated microelectrodes. IrO_x was electrodeposited onto Au nanomesh microelectrodes from a solution prepared in lab using similar recipe from previous report.^[19] The solution preparation started with sequential additions of IrCl_4 (225 mg), 30% hydrogen peroxide (1.386 mL) and oxalic acid dehydrate (750 mg) into deionized water (150 mL). After each addition, the solution was stirred for \approx 20 min at room temperature. Then pH value of solution was slowly adjusted from its initial value (usually \approx 1.4) to 10.5 by adding certain amount of anhydrous potassium carbonate. The mixed solution needs at least 48 h to equilibrate at room temperature prior to use. Deposition of the IrO_x film was performed using galvanostatic mode of Gamry Reference 600+ potentiostat/galvanostat/ZRA (Gamry Instruments, Inc). Here typical three-electrode configuration was adopted including Ag/AgCl reference electrode and Pt counter electrode. The Au nanomesh microelectrode was immersed into the monomer solution as working electrode. 0.5 mA cm⁻² constant current was applied with different deposition time from 25 to 200 s, which resulted in different thicknesses, transmittance as well as electrical characteristics.

X-ray Photoelectron Spectroscopy: X-ray photoelectron spectroscopy (XPS) was employed to determine the elemental composition and bonding states of the samples. The XPS consisted of an Mg/Al dual-anode nonmonochromated X-ray source (Phi model 04-548) and a hemispherical analyzer (Phi model 10-360). The two X-ray options were Mg $\text{K}\alpha$ (1253.6 eV) and Al $\text{K}\alpha$ (1486.6 eV) operated at 300 W. The system was calibrated using Au 4f and Cu 2p, and had a minimum full width half maximum (FWHM) of 1.5 eV with an 80% Gaussian/Lorentzian distribution at a pass energy of 35.75 eV. XPS analysis revealed the chemical composition of a 1 mm circle of the surface to a depth of ≈ 10 nm at a 90° take-off angle.vcx.

Electrochemical Characterization: Both electrochemical impedance spectroscopy (EIS) and cyclic voltammetry (CV) measurement were conducted using Gamry potentiostat. Before measurements, UV/ozone (Bioforce Nanosciences, Inc Procleaner 110) was used to clean microelectrodes for 15 min. Both EIS and CV measurements adopted typical three-electrode configuration, consisting of working electrode (nanomesh microelectrodes), Ag/AgCl reference electrode, and platinum (Pt) counter electrode. Electrodes were immersed in 0.01 M phosphate-buffered saline (PBS) solution for both measurements. Frequencies for EIS swept from 100 Hz to 100 kHz with 10 mV rms AC voltage. Impedance fitting used the Gamry Echem Analyst software (Gamry Instrument, Inc). CV was measured between potential limits of -0.6 and 0.8 V using 50 mV s⁻¹ scan rate. Bench recording of noise were done using Intan stimulation/recording System through immersing nanomesh microelectrodes and Pt reference electrode into PBS solution. Then the recorded noise signal was filtered by 60 Hz notch filter and a 0.1 Hz to 5000 Hz bandpass filter. MATLAB R2016a software (MathWorks) performed data reading/exporting and signal processing by customized coding.

Charge Injection Limit Characterization: Voltage transient measurement was conducted to derive charge injection limit. Also, three-electrode configuration was adopted in 0.01 M PBS solution with Ag/AgCl reference electrode and Pt counter electrode. Intan RHS2116 microchip (Intan Technologies) provided the customized current pulses to stimulate the microelectrodes. All the electrodes in PBS solution were connected to the microchip. The microchip was then connected to the Intan stimulation/recording controller (Intan Technologies),

which was connected to a computer and controlled by a GUI software. The amplitude of current was slowly increased until either E_{ma} reached 0.8 V or E_{mc} of microelectrodes reached -0.6 V, then calculated the charge injection limit using the maximum current we applied. Access voltage (V_a), which represents the voltage drop caused by the ionic conductivity of electrolyte, was considered in the calculation of E_{ma} and E_{mc} . V_a can be estimated from either the onset or end of a current pulse. A common strategy to better locate V_a is to add a short interphase period between two continuous pulses. The largest (smallest) value in a voltage transient curve minus (plus) V_a gives E_{ma} (E_{mc}). In this case, we adopted cathodic first, charge-balanced biphasic current pulse with symmetric 500 μ s width and 66.7 μ s interphase for the charge injection limit characterization. We also applied 0.2–0.8 V positive bias to the microelectrodes versus the Ag/AgCl reference microelectrode to find the maximum charge injection limit since it has been proved that PEDOT:PSS and IrO_x-based microelectrodes benefit from positive bias, and bias-controlled current pulses can be achieved.^[7a,28] Different positive biases were delivered to the microelectrodes by DC power supply across 10 MΩ resistor. Voltage transients under different currents can be found in supporting information (Figure S11a,b, Supporting Information).

Large-Signal Bioimpedance Electrode Model: We derived a large-signal equivalent-circuit model of the electrode by leveraging the stimulation waveform achieved in charge injection limit characterization (Section 4.7) by using a measurement technique^[25] based on time-domain signal analysis. The large signal model differs from results of EIS measurements, which is small signal stimuli based and thus are better suited for study of the recording behavior. The stimulation-response behavior instead follows a waveform described by a standard Randles Cell with the derived equivalent circuit parameters. The large signal model facilitates the study of the electrode behavior during a stimulation current pulse, considering current amplitude and duration, and can be used to predict whether the electrode potential exceeds the water window. Figure 4a for Au NM electrode (black trace) shows a case where the electrode potential approaches the water window and begins to deviate from standard Randles Cell response. The PEDOT and IrO_x coated electrodes closely follow the predicted potential response waveform with a purely capacitive or Faradaic behavior, respectively, and do not exceed the water window limits.

Light-Induced Artifacts Characterization: A dual-LED LEDC2 (Doric Lenses Inc.) connected to Doric fibers delivered light with two different wavelengths (470 nm blue, 590 nm amber) for light induced artifacts characterization. Driving current of the LED ranges from 0 to 1000 mA. The tip of fiber was attached on the microelectrode surface. Intan stimulation/recording system enabled the recording of potential peaks, with bandpass filter from 0.1 Hz to 10 000 Hz and a 60 Hz notch filter.

Supporting Information

Supporting Information is available from the Wiley Online Library or from the author.

Acknowledgements

Y.Q. and K.J.S. contributed equally to this work. This work was supported by Northeastern University. The authors thank the cleanroom staff of George J. Kostas Nanoscale Technology and Manufacturing Research Center at Northeastern University for technical advices on the nanosphere lithography and device fabrication.

Conflict of Interest

The authors declare no conflict of interest.

Keywords

bilayer nanomeshes, iridium oxide, PEDOT:PSS, templated electrodeposition, transparent microelectrodes

Received: July 22, 2017

Revised: August 31, 2017

Published online: November 2, 2017

- [1] D.-W. Park, A. A. Schendel, S. Mikael, S. K. Brodnick, T. J. Richner, J. P. Ness, M. R. Hayat, F. Atry, S. T. Frye, R. Pashaie, S. Thongpang, Z. Ma, J. C. Williams, *Nat. Commun.* **2014**, *5*, 5258.
- [2] M. D. Rugg, M. G. Coles, *Electrophysiology of Mind: Event-Related Brain Potentials and Cognition*, Oxford University Press, New York, NY, USA **1995**.
- [3] T. J. Sejnowski, P. S. Churchland, J. A. Movshon, *Nat. Neurosci.* **2014**, *17*, 1440.
- [4] D. Kuzum, H. Takano, E. Shim, J. C. Reed, H. Juul, A. G. Richardson, J. De Vries, H. Bink, M. A. Dichter, T. H. Lucas, D. A. Coulter, E. Cubukcu, B. Litt, *Nat. Commun.* **2014**, *5*, 5259.
- [5] a) B. A. Wilt, L. D. Burns, E. T. W. Ho, K. K. Ghosh, E. A. Mukamel, M. J. Schnitzer, *Annu. Rev. Neurosci.* **2009**, *32*, 435; b) M. B. Ahrens, M. B. Orger, D. N. Robson, J. M. Li, P. J. Keller, *Nat. Methods* **2013**, *10*, 413; c) M. Böhmer, J. Enderlein, *JOSA B* **2003**, *20*, 554.
- [6] K. Deisseroth, *Nat. Methods* **2011**, *8*, 26.
- [7] a) S. F. Cogan, *Annu. Rev. Biomed. Eng.* **2008**, *10*, 275; b) T. D. Kozai, A. L. Vazquez, *J. Mater. Chem. B* **2015**, *3*, 4965.
- [8] a) P. Ledochowitsch, E. Olivero, T. Blanche, M. M. Maharbiz, presented at *Engineering in Medicine and Biology Society, EMBC, 2011 Annual Int. Conf. of the IEEE* Boston, MA, USA, *8*, **2011**; b) K. Y. Kwon, B. Sirowatka, W. Li, A. Weber, presented at *Biomedical Circuits and Systems Conference (BioCAS)*, 2012 IEEE, Hsinchu, Taiwan, *11*, **2012**; c) N. Kunori, I. Takashima, *J. Neurosci. Methods* **2015**, *251*, 130.
- [9] K. J. Seo, Y. Qiang, I. Bilgin, S. Kar, C. Vinegoni, R. Weissleder, H. Fang, *ACS Nano* **2017**, *11*, 4365.
- [10] R. Paetzold, K. Heuser, D. Henseler, S. Roeger, G. Wittmann, A. Winnacker, *Appl. Phys. Lett.* **2003**, *82*, 3342.
- [11] a) Y. Zhang, S. F. Ali, E. Dervishi, Y. Xu, Z. Li, D. Casciano, A. S. Biris, *ACS Nano* **2010**, *4*, 3181; b) K.-H. Liao, Y.-S. Lin, C. W. Macosko, C. L. Haynes, *ACS Appl. Mater. Interfaces* **2011**, *3*, 2607; c) A. Bianco, *Angew. Chem., Int. Ed.* **2013**, *52*, 4986.
- [12] U. A. Aregueta-Robles, A. J. Woolley, L. A. Poole-Warren, N. H. Lovell, R. A. Green, *Front. Neuroeng.* **2014**, *7*, 15.
- [13] a) X. T. Cui, D. D. Zhou, *IEEE Trans. Neural Syst. Rehabil. Eng.* **2007**, *15*, 502; b) S. Venkatraman, J. Hendricks, Z. A. King, A. J. Sereno, S. Richardson-Burns, D. Martin, J. M. Carmena, *IEEE Trans. Neural Syst. Rehabil. Eng.* **2011**, *19*, 307; c) M. Ganji, E. Kaestner, J. Hermiz, N. Rogers, A. Tanaka, D. Cleary, S. H. Lee, J. Snider, M. Halgren, G. R. Cosgrove, B. S. Carter, D. Barba, I. Uguz, G. G. Malliaras, S. S. Cash, V. Gilja, E. Halgren, S. A. Dayeh, *Adv. Funct. Mater.* **2017**, *1700232*.
- [14] J. D. Weiland, D. J. Anderson, M. S. Humayun, *IEEE Trans. Biomed. Eng.* **2002**, *49*, 1574.
- [15] E. W. Keefer, B. R. Botterman, M. I. Romero, A. F. Rossi, G. W. Gross, *Nat. Nanotechnol.* **2008**, *3*, 434.
- [16] a) R. D. Meyer, S. F. Cogan, T. H. Nguyen, R. D. Rauh, *IEEE Trans. Neural Syst. Rehabil. Eng.* **2001**, *9*, 2; b) S. F. Cogan, J. Ehrlich, T. D. Plante, A. Smirnov, D. B. Shire, M. Gingerich, J. F. Rizzo, *J. Biomed. Mater. Res., Part B* **2009**, *89*, 353; c) S. Negi, R. Bhandari, L. Rieth, F. Solzbacher, *Biomed. Mater.* **2010**, *5*, 015007.

- [17] a) P. Gkoupidenis, N. Schaefer, B. Garlan, G. G. Malliaras, *Adv. Mater.* **2015**, *27*, 7176; b) Y. Xia, K. Sun, J. Ouyang, *Adv. Mater.* **2012**, *24*, 2436.
- [18] S. F. Cogan, T. Plante, J. Ehrlich, presented at *Engineering in Medicine and Biology Society, 2004. IEMBS'04. 26th Annual Int. Conf. of the IEEE*, San Francisco, CA, USA, 11, **2004**.
- [19] K. Yamanaka, *Jpn. J. Appl. Phys.* **1989**, *28*, 632.
- [20] X. Cui, D. C. Martin, *Sens. Actuators, B* **2003**, *89*, 92.
- [21] a) V. Singh, S. Arora, M. Arora, V. Sharma, R. Tandon, *Semicond. Sci. Technol.* **2014**, *29*, 045020; b) S. H. Chang, C.-H. Chiang, F.-S. Kao, C.-L. Tien, C.-G. Wu, *IEEE Photonics J.* **2014**, *6*, 1.
- [22] a) J. Lee, H.-S. Yang, N.-S. Lee, O. Kwon, H.-Y. Shin, S. Yoon, J. M. Baik, Y.-S. Seo, M. H. Kim, *CrystEngComm* **2013**, *15*, 2367; b) D. Chandra, T. Sato, R. Takeuchi, D. Li, T. Togashi, M. Kurihara, K. Saito, T. Yui, M. Yagi, *Catal. Today* **2017**, *3*, 9.
- [23] J. D. Weiland, D. J. Anderson, *IEEE Trans. Biomed. Eng.* **2000**, *47*, 911.
- [24] a) J. D. Weiland, W. Liu, M. S. Humayun, *Annu. Rev. Biomed. Eng.* **2005**, *7*, 361; b) E. Margalit, M. Maia, J. D. Weiland, R. J. Greenberg, G. Y. Fujii, G. Torres, D. V. Piyathaisere, T. M. O'Hearn, W. Liu, G. Lazzi, G. Dagnelie, D. A. Scribner, E. de Juan, M. S. Humayun, *Surv. Ophthalmol.* **2002**, *47*, 335.
- [25] Y.-K. Lo, C.-W. Chang, W. Liu, presented at *Engineering in Medicine and Biology Society (EMBC), 2014 36th Annual Int. Conf. of the IEEE*, Chicago, IL, USA, 8, **2014**.
- [26] H. Lyu, X. Liu, N. Rogers, V. Gilja, D. Kuzum, presented at *Engineering in Medicine and Biology Society (EMBC), 2016 38th Annual Int. Conf. of the IEEE*, Orlando, FL, USA, 8, **2016**.
- [27] B. W. Zeff, B. R. White, H. Dehghani, B. L. Schlaggar, J. P. Culver, *Proc. Natl. Acad. Sci. USA* **2007**, *104*, 12169.
- [28] S. F. Cogan, P. R. Troyk, J. Ehrlich, T. D. Plante, D. E. Detlefsen, *IEEE Trans Biomed. Eng.* **2006**, *53*, 327.